Direct Numerical Simulations of pore competition in idealized micro-spall

Stéphane Zaleski[a], Wojciech Aniszewski[a], Leon Malan[a], Antoine Llor[b]

a. Institut Jean Le Rond d'Alembert -CNRS UMR 7190 - UPMC Paris VI, 4 place Jussieu Paris, France

b. CEA, DAM, DIF - CEA - 91297 Arpajon Cedex, France

Abstract :

Cavitation and micro-spall appear when a weakly compressible liquid is suddenly submitted to large negative pressures resulting in volume growth. After the initial phases of uniform expansion and pore opening, a longer-lasting phase of pore growth and competition appears, which is especially difficult to investigate either experimentally or numerically [1]. Thus this study is among the first of its kind. We present here Direct Numerical Simulations (DNS) of this latter phase for idealized conditions relevant to micro-spall: incompressible inviscid fluid, vanishing vapor pressure in cavities, ballistic uni-axial expansion, perturbed Face-Centered-Cubic arrangement of pores. Under these assumptions, the system is characterized by a single dimensionless Weber number based on the number of pores per unit volume. Volume transfer between pores occurs at low enough Weber numbers; this phenomenon, known as "pore competition" is important as it is drives the temporal evolution of the statistical distribution of pore sizes. Small pores shrink and eventually disappear as their volume is transferred to large pores. Pore statistics and pressure evolution profiles can then be obtained for future modelling purposes. The simulations were performed using the Volume of Fluid method [10] with the mixed-Youngs-central scheme for normal vector computation and interface segment reconstruction, Lagrangian explicit or "CIAM" advection, an original adapted first order extrapolation method in the neighborhood of the free surface, and a ghost fluid method for the pressure boundary condition on the free surface. The pressure used in the boundary condition is computed using Laplace's law, which in turn involves surface tension and curvature. Curvature is computed using the height-function method. The method was tested comparing numerical solutions to solutions of the Rayleigh-Plesset equation for oscillating bubbles. An adapted procedure is used to manage the collapsing cavities. A cavity tagging and Lagrangian tracking algorithm is used to retrieve statistics of cavity sizes. Results indicate that both the uniform growth in the initial expansion phase, as the later "competition" regime can be captured.

Keywords: micro spall, cavity, Volume of Fluid (VOF), Free Surface, pore competition

1   Introduction

Cavitation and micro-spall appear when a weakly compressible (or expansible) liquid is suddenly submitted to large negative pressures resulting in volume growth. After the initial phases of uniform expansion and pore opening, a longer-lasting phase of pore growth and competition appears, which is

especially difficult to investigate either experimentally or numerically [1]. Thus this study is among the first of its kind. We present here Direct Numerical Simulations (DNS) of this latter phase for idealized con- ditions relevant to micro-spall: incompressible inviscid fluid, vanishing vapor pressure in cavities, ballistic uniaxial expansion, perturbed Face-Centered-Cubic arrangement of pores. Under these assumptions, the system is characterized by a single dimensionless group, the Weber number based on the number of pores per unit volume. Volume transfer between pores occurs at low enough Weber numbers, a phenomenon designated as "pore competion". The pore competition effect is important as it is the main phenomenon driving the evolution in time of the statistical distribution of pore sizes. Small pores shrink and eventually dis- appear as their volume is transferred to large pores. Pore statistics and pressure evolution profiles can then be obtained for future modelling purposes.

2   Uni-axial expansion

We investigate a fluid system called "ballistic expansion" in which the mass-weighted average of the velocity field behaves as

$$\mathbf{u}(\mathbf{x}, t) = \mathbf{x}/t \tag{1}$$

in Eulerian coordinates. A uni-axial variant is

$$u(x, t) = x/t \tag{2}$$

In both cases the Lagrangian velocity is constant $\mathbf{U}_a(t) = \mathbf{U}_0$ and the Lagrangian particle position is $\mathbf{U}_0 t$. This solution is a solution of the Euler equation with no pressure term, i.e.

$$\partial_t \mathbf{u} + (\mathbf{u} \cdot \nabla)\mathbf{u} = -\frac{1}{\rho}\nabla p \tag{3}$$

with $p =$Constant. The divergence of the velocity field is:

$$\nabla \cdot \mathbf{u} = d/t \tag{4}$$

where d is the dimensonality of the expansion: we assume $d = 1$ below. This solution may also be called an expansion wave.

Consider now the simulation domain $(-L_0/2, L_0/2)^3$ and simulation time starting at $t = t_1$. Moreover $t = 0$ is the initial time of the expansion. We will define $t_0 > 0$ as the time at which the pores would have zero radius, i.e. cavitation nuclei [3] appear. Further, we assume that the pores are initialized with non-zero radii (which is necessary due to limitations in computational code) i.e. simulations are started at $t_1 > t_0$.

We describe below a model by which one can relate t_0 and t_1. . In the L_0^3 domain, the volume of gas is $V_g(t)$ and the volume of liquid is $V_l(t)$. Obviously $V_g + V_l = L_0^3$ and the average density is $\rho = \rho_l V_l L_0^{-3}$. Making use of the relation for the Lagrangian derivative of ρ:

$$\frac{\mathrm{d}\ln\rho}{\mathrm{d}t} = -\nabla \cdot u \tag{5}$$

we find $\ln\rho = -d\ln t$. Since at t_0 the volume of the cavities is zero, we have $\rho = \rho_l$ and

$$\rho = \rho_l \frac{t_0}{t}. \tag{6}$$

Then $V_l = L_0^3 t_0/t$ and

$$V_g = L_0^3(1 - t_0/t). \tag{7}$$

The number density of pores is also an Eulerian field $N(\mathbf{x}, t)$. Barring coalescence of pores/bubbles this number is just transported as the density and thus

$$\frac{\mathrm{d}\ln N}{\mathrm{d}t} = -\nabla \cdot u \tag{8}$$

which leads to

$$N = N_0 \frac{t_0}{t}. \tag{9}$$

and the volume per bubble is

$$V_b = V_g/N = \frac{L_0^3}{N_0}\left(\frac{t}{t_0} - 1\right) \tag{10}$$

Thus assuming all the bubbles have the same radius $R_b(t)$

$$R_b(t) = L_0 \left(\frac{3}{4\pi N_0}\right)^{1/3}\left(\frac{t}{t_0} - 1\right)^{1/3} \tag{11}$$

The distance ℓ_d between bubbles grows like

$$\ell_d = \frac{L_0}{N_0^{1/3}}\left(\frac{t}{t_0}\right)^{d/3} \tag{12}$$

Equations (11) and (12) can be rephrased in a form binding bubble radii with inter-bubble distances:

$$\frac{\ell_d(t)}{R_b(t)} = \sqrt[3]{1 - \frac{t_0}{t}}. \tag{13}$$

3   Weber number

In general, the dimensionless Weber number We is defined as ratio E_K/E_S where E_K is the kinetic energy of bubble expansion or collapse and E_S is the surface energy. Seeing as we have $E_S = 4\pi\sigma R_b^2$ and $E_K \sim (4\pi/3)\rho \dot{R}_b^2 R_b^3$, the ratio takes the form:

$$\mathrm{We} \sim \frac{\rho \dot{R}_b^2 R_b}{3\sigma}, \tag{14}$$

which we can also express in terms of "pure" time dependency, i.e. with t as the only independent variable, using formulae (11) and (12). For this, we first define the *initial* Weber number We_0 as

$$\mathrm{We}_0 = \frac{3\rho}{8\pi\sigma n t_0^2}. \tag{15}$$

(In above t_0 is the aforementioned moment at which bubbles have zero radius). For uni-axial expansion, we can then define:

$$\mathrm{We}(t) = \frac{t_0\left(\sqrt[3]{1 - \frac{t_0}{t}} - 1\right)}{t - t_0} \tag{16}$$

thus suggesting that the Weber number should decay with time as t^{-2} at large t. Due to the decrease, we expect to observe changing regimes: from convection dominated (quenched competition, which we term "isolation") to free pore competition.

With this simple model the initial conditions are

$$R_b(t_1) = L_0 \left[\frac{3}{4\pi N_0} \left(\frac{t_1}{t_0} - 1 \right) \right]^{1/3} \tag{17}$$

for the initial pore radii at the moment t_1 when the simulation is initialized.

In computational practice, it is desirable for $R_b(t_1)$ to be small, to offer a large range of scales. Ideal relation would be:

$$\Delta x \ll R_b(t_1) \ll \ell_d \ll L_0. \tag{18}$$

where Δx is the grid size. The leftmost and rightmost inequalities of (18) are however slightly relaxed for the results presented in this paper due to grid resolutions used, as will be detailed below.

4   Computational Methods

Parallel Robust Interface Simulator (PaRIS) is an in-home CFD code developed at Institute ∂'Alembert. A well known projection scheme [10] is used to solve momentum conservation equations. Starting with the definition of the temporary velocity field $\mathbf{u}^*$:

$$\frac{\mathbf{u}^* - \mathbf{u}^n}{\Delta t} = -\mathbf{u}^n \cdot \nabla_h \mathbf{u}^n, \tag{19}$$

which can be found easily as the only unknown in above formula. Symbol ∇_h stands for the discrete differential operator. This is a *projection* step since velocity is projected onto a space with zero pressure field.

Subsequently, the pressure field at the end of the time-step p^{n+1} is found using $\mathbf{u}^*$ from (19), original Euler equation (3) and the discrete version of the impressibility condition (4):

$$\nabla_h \cdot \left[\frac{\Delta t}{\rho^n} \nabla_h p^{n+1} \right] = \nabla_h \cdot \mathbf{u}^* + \nabla_h \cdot \left(\frac{\Delta t}{\rho^n} \sigma \kappa \mathbf{n} \delta_s \right), \tag{20}$$

where superscript $n+1$ stands for the value at the end of n-th time-step. In most computational codes, and no different in Parisimulator, numerical solution of the above equation (discrete Poisson equation) is the part of the solution to which most computational cost is associated: up to 90 percent. Once (20) is solved with p^{n+1} found, both it and $\mathbf{u}^*$ are used to find the divergence-free velocity at the end of the time-step:

$$\mathbf{u}^{n+1} = \mathbf{u}^* - \frac{\Delta t}{\rho_n} \left(\nabla_h p^{n+1} + \sigma \kappa \mathbf{n} \delta_s \right) \tag{21}$$

thus ending the procedure. As mentioned, normal vectors $\mathbf{n}$ and curvatures κ in above equations[1] are

---

[1] The same applies for the approximation of Dirac delta δ_s.

found from the color/fraction function c, whose advection equation follows in discrete form:

$$\frac{c^{n+1} - c_n}{\Delta t} + \nabla_h \cdot (c\mathbf{u}^n) = 0. \tag{22}$$

Above equation cannot be solved directly, as c is a sharp jump function: the jump would be diffused by numerical errors [12]. Therefore, in most applications (22) is solved using specially crafted geometrical reconstruction/advection schemes such as CIAM [6] or PLIC [2]. Normal vectors and curvature are calculated using Height Functions technique [4, 9] which has multiple provisions for the cases of insufficient grid resolutions or specific interface configuration.

To implement the boundary conditions on the interface, Free Surface method has been implemented in Parisimulator [7]. The flow withing the pores is not solved for (except up to two interior cell layers as explained below), which amounts to representing their contents as vacuum. With that assumption the flow is in fact a single phase flow, surface tension is accounted for on the pore surfaces.

1. Pressure field is extrapolated onto the interface which is necessary for (20). The boundary value of the gradient is computed as

$$p^* = p_b - \sigma\kappa,$$

where p_b is constant pore pressure, and $\sigma\kappa$ is Laplace pressure, thereby assuring that surface tension effect is accounted for. The p^* value is used for ∇_h operators for cells neighbouring the interface;

2. The velocity field is extrapolated within the pores; these values are necessary for higher-order gradient operators for cells neighbouring the interface. Extrapolation is based on liquid velocity, which is extended to two grid-cell layers (or 'levels') within pore/bubble interior by geometrical fitting and least-squares minimization;

3. Finally, the extrapolated velocities in level 1 and 2 cells are corrected to ensure the new field is divergence free.

5   Simulation Setup

To simulate the idealized micro-spall phenomenoa in a way specified in Section 2 we have set up the simultions in a following way. Cubical computational domain is used, containing a given number of pre-seeded bubbles in a FCC (Face-Centered Cubic) lattice. The domain is expanded in x direction as assumed in Section 2. More specifically, the proper temporal evolution of the velocity field described by (1) is ensured by:

- Initializing the x-velocity component to $u = x$ with proper translation and scaling, so that for $t = t_1$ we have $u(0, t_1) = -u_n$, $u(L/2, t_1) = 0$ and $u(L, t_1) = u_n$ where u_n is the outflow velocity;

- initializing the outflow boundary condition for the velocity field $\mathbf{u} = (u, v, w)$ in such manner, that

$$u_n = 1/t_1 \tag{23}$$

where $t_1 > 0$. For subsequent moments of simulated time t (23) is held so that $|u_n(t)| = 1/t$ at all times;

Table 1: Parameter table for two example simulations of the uni-axial expansion, as explained in the text.

label	ρ	σ	t_1	t_0	var (r)	We (t_1)	Ma (t_1)
I	1000	0.1	$8 \cdot 10^{-2}$	$7.797 \cdot 10^{-2}$	50%	512.83	15
C	444	1	2.1	2.092	50%	$3.3 \cdot 10^{-2}$	0.12

- For v and w components, defining initial values to zero.

Periodic boundary conditions are imposed on YZ walls. For the condition to be compatible with the bubble cluster geometry, it is re-shaped by adjusting the bubble-free buffer surrounding it. Cubic domain of size $L = 1$ is assumed with initially 355 bubbles. We describe simulation results concerning the uni-axial expansion using example simulations whose parameters are given in Table 1.

Example simulations have been performed using 256^3 grid points. For the first simulation ("I"), value of Weber number 16 at t_1 is 512.83. The bubble lattice is configured as specified above, with liquid characteristics found in Table 1. In the Table, "I" and "C" are labels designating the "Isolation" and "Competition" regimes; We and Ma are dimensionless Weber and Mach numbers, ρ and σ are respectively liquid density and surface tension applied at the pore surfaces, while var(r) stands for the a variation in pore radii applied to the initial condition.

Due to the applied spatial resolution, certain restrictions on the initial bubble radii $R_b(t_1)$ are imposed, as the bubbles must be resolved (i.e. properly represented by the interface tracking methods) at t_1.

Note that by (17) we have:

$$R_b(t) = L_0 \left(\frac{3}{4\pi N_0} \right)^{1/3} \left(\frac{t}{t_0} - 1 \right)^{1/3} \tag{24}$$

Which applies as well to t_1. Having the size of domain L_0 and initial pore number N_0 fixed, and imposing additional restriction $R_b > 3\Delta x$ (to make sure the initially small pores are properly represented by the VOF method) we choose $t_1 = 0.08$ for the presented simulation. This amounts to $R_b t_1/\Delta x \approx 3.44$ which, is considered resolved[10] in that proper values of curvature can be computed for bubbles of that radius[2]. Due to the above dependence between simulation initial time t_1 and bubble radii, any decrease of t_0, and t_1/t_0 would reduce R_b, which in turn would imply an increased grid resolution.

6 Results

6.1 Isolation regime

Figure 1a presents cluster geometry at $t' = t_1 + 1.929 \cdot 10^{-2}$. Uniform expansion of the bubbles/pores is clearly visible with pore layers closest to the walls along the x axis visibly elongated due to the fact that convection is strongest there. At $t \geq t_1 + 1.92 \cdot 10^{-2}$ one observes bubble radii of order of ℓ_d. Nearly all pores are ellipsoidal in shape, and have expanded beyond the region of the simulated volume, including periodic yz walls. Moreover, the outer layer of pores has now completely disappeared (been convected out) from the simulation, as only remnant interfacial cells are visible.

The pore volume fraction using (7) with a value of $t_1 = 0.08$ should be $3.59 \cdot 10^{-3}$, however is slightly lower in simulation, due to the initial variance in pore radius (Table 1) introducing additional volume.

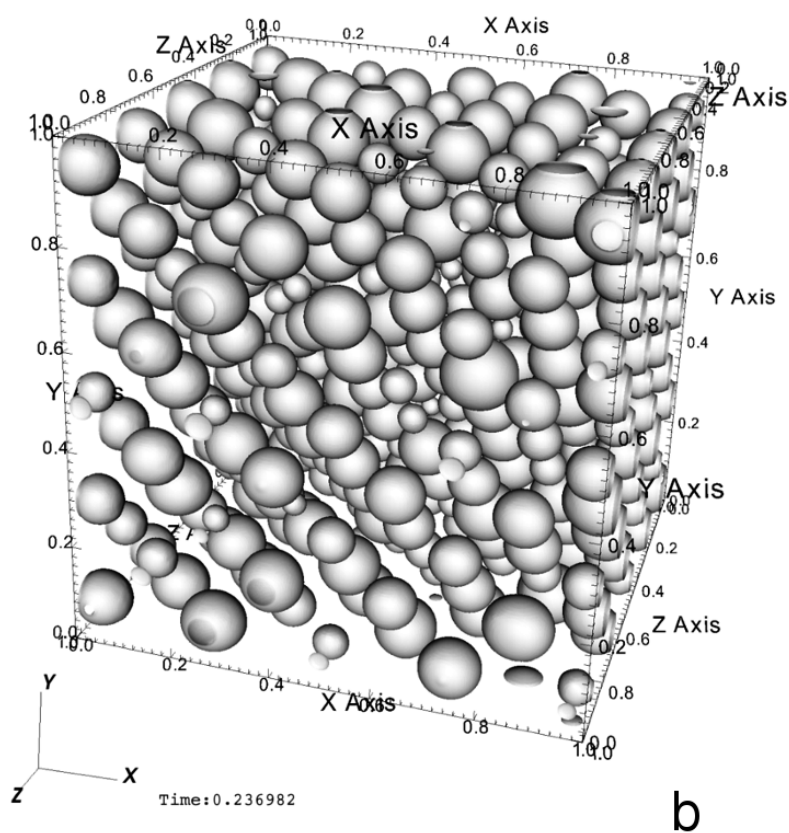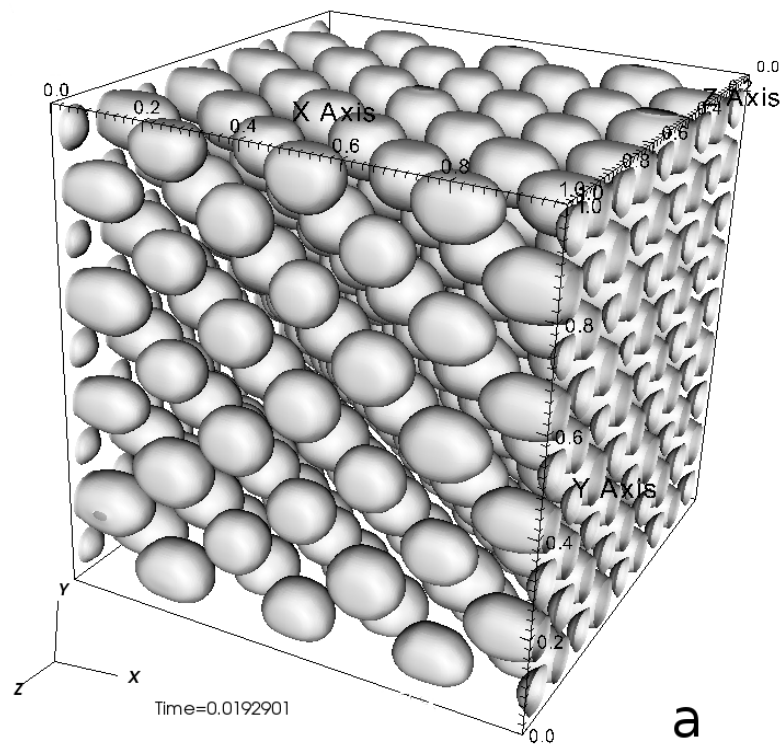[2]Not accounting for about 5 percent variance in R_b in init.

Figure 1: (a) Simulation of the flow characterized by $We = 512$. ("isolation" regime) at $t = t_1 + 1.92 \cdot 10^{-2}$. (b) Simulation of the pore lattice at $We = 3.3 \cdot 10^{-2}$ ("competition" regime) for $t = t_1 + 0.237$.

Proper scaling has thus been used for the analytic formula to make up for that. Another source of a difference between (7) and simulatied pore volue is that thepores leave the computational domain as they are expanded (which in the "I" simulation takes place at $t + t_1 > 0.05$).

6.2   Competition regime

We continue the description of the results with the second simulation ("C") which, as seen in Table 1 is characterized by much lower Weber number. As a result of this, the evolution of the pore lattice is no more dominated by expansion and the pores are not isolated, and the elongated shapes of the pores visible in Figure 1a give way to a "pore competition" phenomenon. As visible in Figure 1b, number of pores has either shrunk or is at the verge of imploding, their volume being overtaken by a group of large pores. Distribution of radii in the latter group is rather isotropic with all pores roughy spherical and spheroidal forms absent. Figure 1b contains also back-dropped planes coloured using the pressure field, which for $t = 2.4$ has near-zero values. This is due to the fact that positive pressure field is associated with expanding liquid, while for low Weber number negative Laplace pressures (capillary force) dominate the pressure distribution.
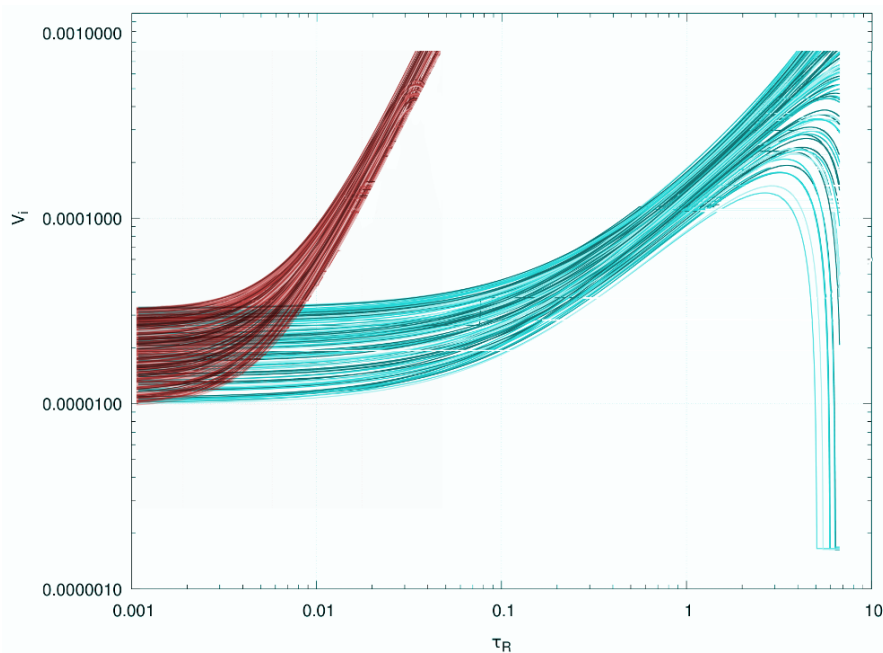

Figure 2: Pores volumes history for $We = 512$ (brown), and $We = 0.03$ (blue) flows.

The implosion events are visible also in Figure 2 which displays individual pore volume histories for the larger (brown lines) and smaller (blue lines) Weber numbers. To the accuracy allowed by post-processing software, each line displays volume of an individual pore, with about 300 pores tracked for each simulation. Time is normalized by capillary timescale

$$\tau_R = \left(\frac{\rho R^3}{\sigma} \right)^{1/2} \tag{25}$$

which results (due to parameters presented in Table 1) in factor of 5 between two simulations presented in Figure 2, accounted for in the Figure. Unlike the high-We regime, in which expansion is rapid and nearly uniform, the low-We regime exhibits higher variance in pore volumes, with a number of

implosion events visible towards the end of recorded time. This proves that the presented numerical method is capable of capturing the transition between the two regimes, provided the simulation covers a sufficient temporal range.

References

[1] T. de Rességuier, L. Signor, A. Dragon, G. Roy Dynamic fragmentation of laser shock-melted tin: experiment and modelling *International Journal of Fracture*, 1:109-119, 2010.

[2] W. Aniszewski, T. Ménard, and M. Marek. Volume of fluid (VOF) type advection methods in two-phase flow: A comparative study. *Computers & Fluids*, 97(0):52 – 73, 2014.

[3] G.K. Batchelor. *An Introduction to Fluid Dynamics*. Cambridge University Press, 1967.

[4] S. Cummins, M. Francois, and D. Kothe. Estimating curvature from volume fractions. *Computers and Structures*, 83:425–434, 2004.

[5] J. Delhaye. Jump conditions and entrophy sources in two-phase systems. local instant formulation. *International Journal of Multiphase Flow*, 1:395–409, 1973.

[6] J.Li. Calcul d'interface affine par morceaux. *C.R. Acad.Sci.Paris, série IIb*, 320:391–396, 1995.

[7] Léon Malan and Stéphane Zaleski. Numerical simulation of bubble competition during micro-spalling. Technical Report 13-39-C-DSPG/CAJ, Institut Jean Le Rond d'Alembert, 2015.

[8] M.S. Plesset and A. Prosperetti. Bubble dynamics and cavitation. *Annual Reviews of Fluid Mechanics*, 9:145–185, 1977.

[9] S. Popinet. Gerris: a tree-based adaptive solver for the incompressible euler equations in complex geometries. *Journal of Computational Physics (submitted)*, 2003.

[10] G. Tryggvason, R. Scardovelli, and S. Zaleski. *Direct Numerical Simulations of Gas-Liquid Multiphase Flows*. Cambridge Monographs, 2011.

[11] G.D. Weymouth and D. Yue. Conservative Volume-of-fluid method for free-surface simulations on cartesian grids. *Journal of Computational Physics*, 229:2853–2865, 2010.

[12] D. Youngs. Numerical simulation of turbulent mixing by rayleigh-taylor instability. *Fronts, Interfaces and Patterns*, page 32, 1984.